Max H2 DR

Maximise H2 Enrichment in Direct Reduction Shaft Furnaces

New kinetic models for the reduction of iron ore in H_2-rich atmosphere

Deliverable D1.3 by WP1. Partners: UL, AAU, M21

Antoine Marsigny, Henrik Saxén, Fabrice Patisson

February 2024

This project has received funding from the European Union under grant agreement NUMBER — 101058429 — MaxH2DR

Table of contents

List of Figures

1. Introduction

The present Deliverable reports the work carried out by UL and AAU within the frame of the task 1.3 “Development of kinetic sub-models for H_2-renriched DR” of the work package 1 “New fundamental knowledge and sub-models” for the first 21 months of the MaxH2DR project.

A sizeable modelling work is planned for the project: different types of models (Finite Volume Model, Finite Element Model, Discrete Element Model) for the simulation of a H2-enriched DR (Direct Reduction) shaft reactor, as well as systems models based on global mass and heat balances for DR plant simulation. Those models need to rely on a accurate description of the iron ore reduction reaction kinetics. This description will be based on kinetic sub-models simulating the transformation of iron ore grains and pellets, the sub-models being implemented in the reactor and plant models.

Task 1.3 is devoted to the development of these kinetic sub-models. In addition to be necessary to the reactor and plant models, the kinetic models are also useful to help determining the proper intrinsic kinetic parameters from a comparison between the measured (Task 1.1) and calculated (Task 1.3) data.

Considering the experiments carried out on different scales (grain bed, single pellet, pellet bed) two types of kinetic models have been developed: a grain and powder bed model by AAU and a single pellet model by UL.

The present report describes both models, from their basic principles to the results obtained so far.

2. Modelling fundamentals

2.1. Grain and powder bed model

To be able to interpret the results of the reduction experiments, a mathematical model of the reduction of small fines in a bed was developed. The particles were described by a three-interface shrinking core model (Figure 1) where the reduction degree (X) of the different iron oxides (Fe_2O_3, Fe_3O_4, FeO) along the axial coordinate of the bed (z) was expressed by the differential equations

$$\frac{\partial X_j(t,z)}{\partial t} = \frac{r_j(t,z)}{n_0 \cdot a_j} \quad (eq.1)$$

where t is time and n_0 is the initial oxygen content, while $r_j(t,z)$ is the reaction rate at the three ($j = 1,2,3$) interfaces. Applied to hydrogen reduction, we have

$$r_j(t,z) = \frac{P}{RT}\frac{3}{r_0}\frac{1}{A_j(t,z)|_f} \cdot \left(\frac{N_j(t,z)|_f}{W(t,z)|_f} - y_{H_2,j,eq}(t,z) \right) \quad (eq.2)$$

where R is the gas constant, r_0 is the radius of the initial particle, $y_{H_2,j,eq}$ is the equilibrium molar fraction of H_2 for the *j*-th reaction, while *P* and *T* are the operating pressure and temperature, respectively. $y_{H_2,j,eq}$ is calculated for each reaction front according to

$$y_{i,j,eq}(t,z) = \frac{1}{1+K_j} \cdot \left(y_{H_2,j}(t,z) + y_{H_2O,j}(t,z) \right) \quad (eq.3)$$

where $y_{H_2,j}$ and $y_{H_2O,j}$ represent the molar fractions of the gaseous reactant and product at a given reaction front, while K_j is the equilibrium constant of the j:th reaction.

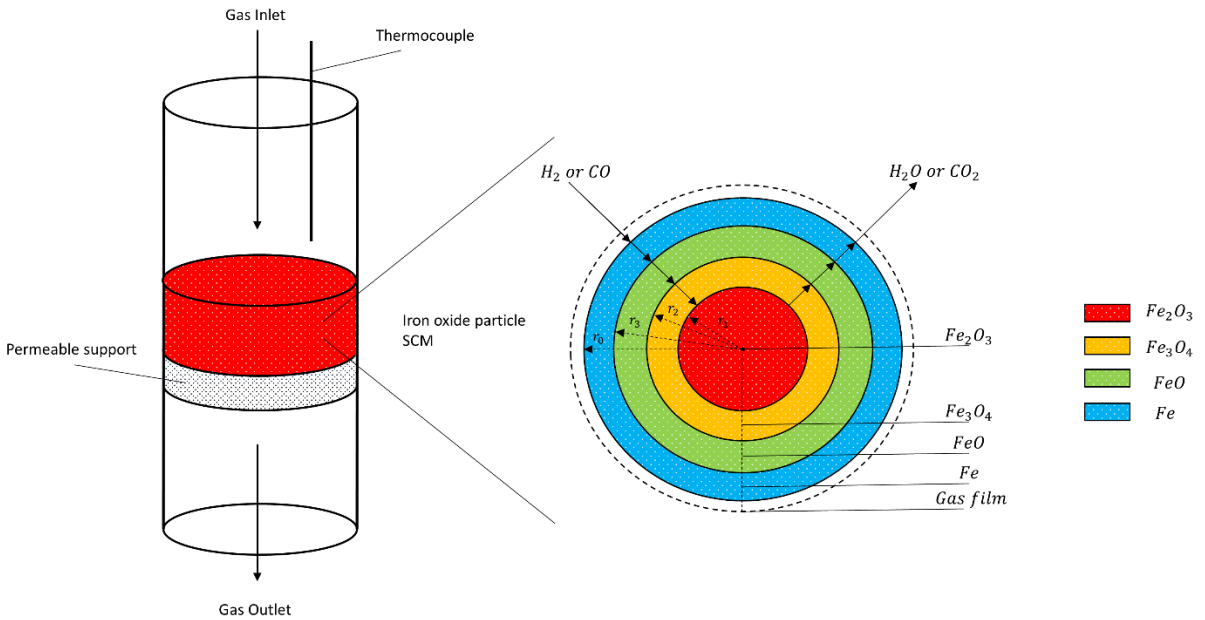

Figure 1. Three-interface shrinking core particle in contact with a reducing gas in a bed.

Starting from the reduction of hematite, the reactive network moves from an initial phase, in which all three reaction fronts are present, to the next phase after the complete reduction of hematite ($X_1(t,z) = 1$) in which only two fronts are present. Similarly, when the magnetite reduction is completed ($X_2(t,z) = 1$), there is a transition to a single-front system. In general, the formulations of the coefficients A_j, W_j, and N_j that define the reduction rate must necessarily change as a function of the number of possible reductions ($A_j(t,z)\big|_f$, $W_j(t,z)\big|_f$ and $N_j(t,z)\big|_f$). The value of the parameter f, which is defined in the system of equations (4) below, is the number of reaction fronts at the time t and the axial coordinate z

$$\textbf{if } \begin{cases} \boldsymbol{X_1(t,z) < 1} & \boldsymbol{f = 3} \quad \boldsymbol{j = 1,2,3} \\ \boldsymbol{X_1(t,z) = 1 \wedge X_2(t,z) < 1} & \boldsymbol{f = 2} \quad \boldsymbol{j = 2,3} \\ \boldsymbol{X_1(t,z) = 1 \wedge X_2(t,z) = 1 \wedge X_3(t,z) < 1} & \boldsymbol{f = 1} \quad \boldsymbol{j = 3} \end{cases} \qquad (\boldsymbol{eqs}.4)$$

N_j represents the effective reduction contribution of each reaction, while W is the total resistance of the system, given by quite complex equations considering also mass transfer resistances.

In expressing the reaction rates, the kinetic factors were written as

$$\boldsymbol{k_j = k_{j,\mathrm{ref}} \cdot \exp\left[\left(-\frac{E_{a,j}}{R}\right)\cdot\left(\frac{1}{T} - \frac{1}{T_{\mathrm{ref}}}\right)\right]} \qquad (\boldsymbol{eq}.5)$$

where $k_{j,\mathrm{ref}}$ and $E_{a,j}$ are the pre-exponential factor and activation energy, respectively, of the j:th reduction reaction used in a modified Arrhenius equation, where T_{ref} is a reference temperature.

Gas composition gradients in the bed (cf. left panel of Figure 1) are described by

$$\frac{\partial c_i(t,z)}{\partial t} = \underbrace{-\frac{u}{h}\cdot\frac{\partial c_i(t,z)}{\partial z}}_{\textbf{Convection}} + \underbrace{\frac{D_z}{h^2}\cdot\frac{\partial^2 c_i(t,z)}{\partial z^2}}_{\textbf{Axial dispersion}} + \underbrace{\frac{1}{(1-\varepsilon)}\cdot\sum_{j|_f}^{3}\nu_{i,j}\cdot r_j(t,z)}_{\textbf{Reaction SCM}} \qquad (\mathbf{eq}.6)$$

In this differential equation, u is the gas velocity, h is the bed height, D_z is the axial dispersion coefficient, ε is the bed voidage and $\nu_{i,j}$ is the stoichiometric coefficient of gaseous species i in reaction j.

The boundary conditions of the differential equation (6) above are

$$\boldsymbol{c_i(t,z)\big|_{z=0} = c_{i,\mathrm{in}}} \qquad \boldsymbol{\left.\frac{\partial c_i(t,z)}{\partial z}\right|_{z=1} = 0} \qquad (\boldsymbol{eq}.7)$$

i.e., given inlet concentrations and no concentration gradient at the end of the bed.

To provide an interpretation by the model of the measured thermal conductivity signals in the experiments, a relation between the gas composition and the thermal conductivity was implemented in using the expression

$$\boldsymbol{\lambda_i = \frac{g_{1,i}\cdot(T/\mathrm{K})^{g_{2,i}}}{1 + \frac{g_{3,i}}{(T/\mathrm{K})} + \frac{g_{4,i}}{(T/\mathrm{K})^2}}} \qquad (\boldsymbol{eq}.8)$$

taken from CHEMCAD, with the parameter values for $g_{1,i}$, $g_{2,i}$, $g_{3,i}$ and $g_{4,i}$ also taken from the same source, where i denotes the chemical component in the gas phase.

The model is described in detail in a recent journal publication. (E. Salucci, 2024).

2.2. Kinetic model of a single pellet

2.2.1. Basics on gas-solid reactions

An introduction to gas solid reactions is given by Szekely et al. (J. Szekely, 1976). In this report, we will take a generic gas-solid reaction to serve as an example :

$$\mathbf{A}_{(g)} + \mathbf{bB}_{(s)} = \mathbf{cC}_{(g)} + \mathbf{dD}_{(s)} \quad (\mathbf{eq}.9)$$

On a microscopic level, a reaction between a gas and a solid involves complex mechanisms that can be summarized with these consecutive steps:

- The diffusion of the gas reactant through the bulk of the gas until it reaches the external surface of the solid reactant, which is usually called “external mass transfer”.
- The diffusion of the gas reactant through the pores of the solid, which is either partially or completely reacted. If the product layer is dense, one can observe a solid diffusion of adsorbed species.
- The adsorption of the gas reactant and the desorption of the gas product.
- The “local chemical reaction”, that is the proper chemical reaction between the gas and the solid.

With the goal of determining the kinetics of a gas-solid reaction, one needs to assess the rate of each of these phenomena, their interplay, and the influence of chemical variables. We expect from the model we have developed that it can simulate the reduction of one single pellet at a constant reaction temperature (assuming the reaction is isothermal at the pellet scale), but we are also interested in studying the effect of gas composition, solid phase distribution, gas flow, gas pressure, etc. A further sophistication might involve studying the mesoscale morphology (that is mostly the microstructure, but also the influence of cracks, dislocations and every kind of defect) – as well as the presence of impurities.

Mass transfer in gas-solid reactions

Following the notations of eq. 1 above, let us define the following quantities:

N_A, the flux of the reactant gas from the bulk into the solid external layer;

C_A, the concentration of the reactant gas gas. It varies between its bulk concentration C_{A0} and its concentration at the solid surface C_{As}.

h_D, a mass transfer coefficient which relates to the Sherwood number N_{Sh}.

The diffusion of reactant from the bulk of the gas to the solid external layer (and the diffusion of gas product from the layer to the bulk) obeys transport equations including both convection and diffusion of the species. The mass transfer equation gives, in its integral form :

$$\boldsymbol{N_A} = \boldsymbol{h_d}(\mathbf{C_{As}} - \mathbf{C_{A0}}) + \boldsymbol{X_{As}}(\boldsymbol{N_A} + \boldsymbol{N_C}) \quad (\mathbf{eq}.10)$$

where X_{As} is the molar fraction of A at the solid surface. In our case of interest, since all reduction equations (see equations below) relate to equimolar counterdiffusion ($\nu_{H_2,i} = \nu_{H_2O,i}$), this boils down to :

$$N_A = h_d(C_{As} - C_{A0}) \quad (eq.11)$$

h_D can be fairly accurately determined from empirical correlations. For the reduction of a spherical pellet in a thermobalance, we use the correlation of Ranz and Marshall. It involves the Schmidt and Reynolds numbers (N_{Sc} and N_{Re}, resp.):

$$N_{Sh} = 2.0 + 0.6 * N_{Re}^{\frac{1}{2}} * N_{Sc}^{\frac{1}{3}} \quad (eq.12)$$

$$N_{Sh} = h_D * \frac{L}{D} \quad (eq.13)$$

Pore diffusion

Compared with molecular diffusion, pore diffusion includes complicating factors, such as the presence of non-straight solid pore walls (described with tortuosity τ), a shift in the diffusion regime depending on the pore width (transition from molecular to Knudsen diffusion), and a potential pressure gradients within the pore.

To account for these phenomena, we use a model which incorporates both molecular and Knudsen diffusions as parallel resistances, while including both porosity and tortuosity:

$$D_{A,eff} = \frac{\epsilon}{\tau} * \left(\frac{1}{D_{A,Knu}} + \frac{1}{D_{A,mix}}\right) \quad (eq.14)$$

where $D_{A,mix}$ is the molecular diffusion of A in the gas mix. It comprises the molar fractions of each gas j and their binary diffusion coefficient with A (the latter is derived from the Chapman-Enskog theory). On the other hand, the Knudsen diffusion coefficient can be readily calculated from :

$$D_{A,Knu} = \frac{d_{pores}}{3} * \sqrt{\frac{8RT}{\pi M_A}} \quad (eq.15)$$

where d_{pores} is the mean diameter of the pores, R is the ideal gas coefficient and M_A is the molecular mass of gas A.

Local chemical reaction

Three factors may be rate-limiting when trying to determine the rate of the local chemical reaction: the adsorption of the reactant gas A, the desorption of the product gas C, or the surface reaction. In systems displaying a shrinking core behaviour, the local rate of a chemical reaction can be defined as the rate of disappearance of A at the surface:

$$R_s = k(T) * \left[C_{As}^n - \left(\frac{C_{Cs}^m}{K_{eq}}\right)\right] \quad (eq.16)$$

in $mol_A\ s^{-1}\ m^{-2}$, where K_{eq} is the thermodynamic equilibrium constant, k is a rate constant, n and m are reaction orders.

A proper determination of the reaction kinetics lies in a rigorous estimation of the rate constant

$$k(T) = k_0\ exp\left(-\frac{E_a}{RT}\right) \quad (eq.17)$$

When a reaction is multi-step, one may want to use multiple rate constants rather than having varying activation energies E_a. Now that the basic principles of gas-solid reactions have been recalled, we can review the gas-solid reaction models most used in the literature, starting with one of the simplest: the shrinking-core model (SCM).

2.2.2. SCM and 3-interface SCM

As explained above, we assume that the chemical reaction takes place at a well-defined interface, namely if the system exhibits a topochemical behaviour. Considering the global reaction reduction of iron oxides :

$$\boldsymbol{Fe_2O_3 + 3H_2 = 2Fe + 3H_2O} \quad (\mathbf{eq}.\,18)$$

We define an interface between the reacted solid product layer made of iron and the unreacted shrinking core made of hematite, as outlined in **Erreur ! Source du renvoi introuvable.**. This allows f or an easier definition of the reaction rate (see eq.8 above).

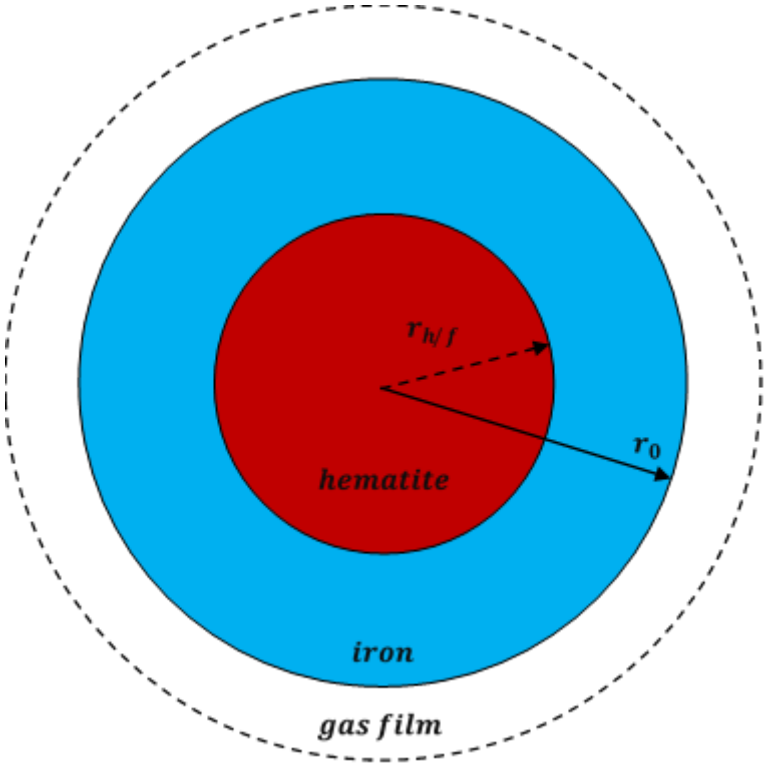

Figure 2. SCM model applied to the reduction of an iron ore pellet. Only the global reduction reaction is considered here.

Depending on which gas-related physical phenomenon is rate-limiting (either mass transfer, pore diffusion or local chemical reaction), we can assume that the rate of the limiting phenomenon equals that of disappearance of the solid (see Table 1), that is:

$$\mathbf{R_{disapp}} = \boldsymbol{\rho_s} \frac{\mathbf{dr_c}}{\mathbf{dt}} (\mathbf{eq}.\,19)$$

Rate limiting phenomenon	Governing equation
Local surface reaction	$\rho_s \frac{dr_c}{dt} = k\left[C_{As}^n - \left(\frac{C_{Cs}^m}{K_{\text{eq}}}\right)\right]$
External mass transfer	$\rho_s \frac{dr_c}{dt} = h_D\left[C_{A0} - \left(\frac{C_{C0}}{K_{\text{eq}}}\right)\right]\left[\left(\frac{K_{eq}}{1+K_{\text{eq}}}\right)\right]$
Gas diffusion through the pores	$-4\pi r_c^2 \rho_s \frac{dr_c}{dt} = b4\pi r^2 D_e \frac{dC_A}{dr} = \frac{4\pi b D_e}{\frac{1}{r_c} - \frac{1}{r_0}}\left[C_{A0} - \left(\frac{C_{C0}}{K_{\text{eq}}}\right)\right]\left[\left(\frac{K_{eq}}{1+K_{\text{eq}}}\right)\right]$

Table 1: Governing equations in the case of a shrinking core behaviour

where $r_c = r_{h/f}$ and ρ_s is the apparent molar density of hematite in the example. We then rearrange these equations into dimensionless forms to obtain a relationship between X and t, which will serve as the basis for building the reduction curves.

*

The 1-interface SCM has been used with some success in the modelling of a direct reduction shaft furnace by (D. R. Parisi, 2004). However, it is quite impractical since it does not allow for the definition of a constant activation energy all along the reaction, which is due to the multi-step nature of iron oxide reduction. Moreover, there is are impressive discrepancies in the values of this activation energy, depending on the experimental conditions.

A more adapted model for the description of the reduction of iron oxides is the 3-interface shrinking core model, as represented in **Figure 3**. Here, we define an interface for each couple of successive oxides, and a partial pressure for both reactant and product gas. The model is adapted from the 1 interface SCM and is explained in details in the previous section, as well as in the original article from (Q. T. Tsay, 1976).

Even though, in the reduction experiments of industrial iron ore pellets, one observes no real successive nor uniform reaction fronts as described in by the 3-interface model (on this matter see the article from (Costa, Modelling a new, low CO2 emissions, hydrogen steelmaking process, 2013)). This is a difference between the grain scale and a pellet scale. We thus need a more complicated model that takes into account the contribution of each phenomenon as well as the description of the pellet inner structure.

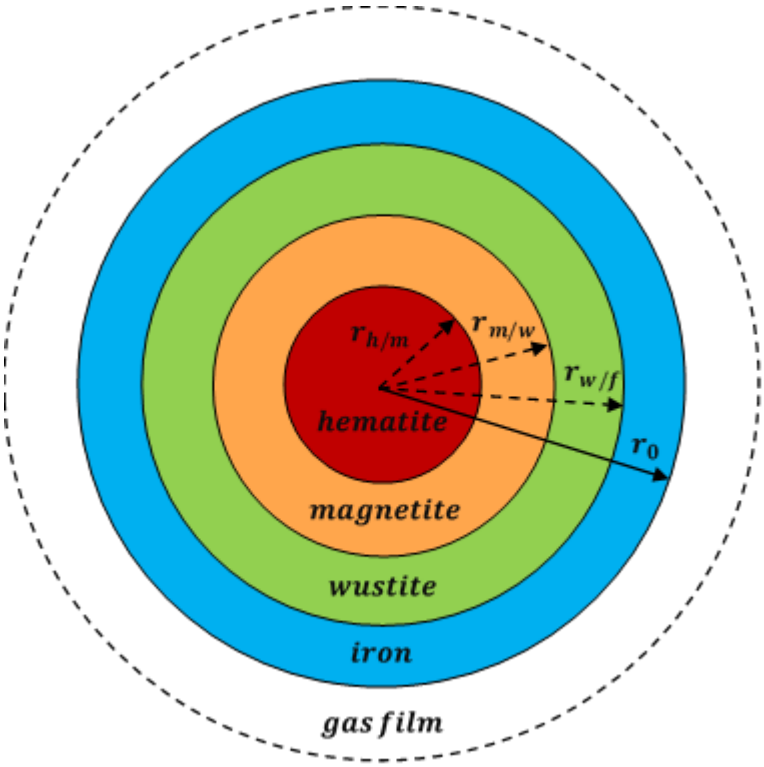

Figure 3. Three interface SCM model applied to the reduction of an iron ore pellet. All consecutive reduction reactions taking place are considered.

2.2.3. Choice of the Grain Model (GM)

The following describes the reduction of a single pellet according to the Grain model (Szekely et al., 1976) and the law of additive reaction times proposed by (Sohn, 1978), as well as our own SPKM (Single Pellet Kinetic Model) model based on these.

The Grain model describes the reaction of a reactant gas with a spherical pellet. The latter is itself made up of spherical grains (see Figure 4. To assess the reduction behaviour of the pellet and calculate the overall reduction, the model considers there are three physical phenomena which can be rate-limiting: the transport of reactant gas (H_2 or CO) from the bulk of the gas to the boundary layer of the pellet, the diffusion of this gas through the pores of the pellet, and the local chemical reaction between the gas and the iron oxide grains. The full Grain model requires a numerical integration of the mass balances of the species along the pellet radius.

However, the influence of each phenomena on the reaction rate can be quantified through a characteristic time τ, expressed as:

$$\tau = \frac{\rho_s \cdot d_s}{k \cdot f_m} \quad (\mathbf{eq}.\,20)$$

where ρ_s and d_s are solid characteristic density and diameter (ρ_s and d_s are not necessarily the solid true density and pellet diameter – the complete description of each τ and other kinetic parameters is left to the interested reader in Ranzani da Costa (2011), k is a kinetic factor and f_m is the driving force of the reaction.

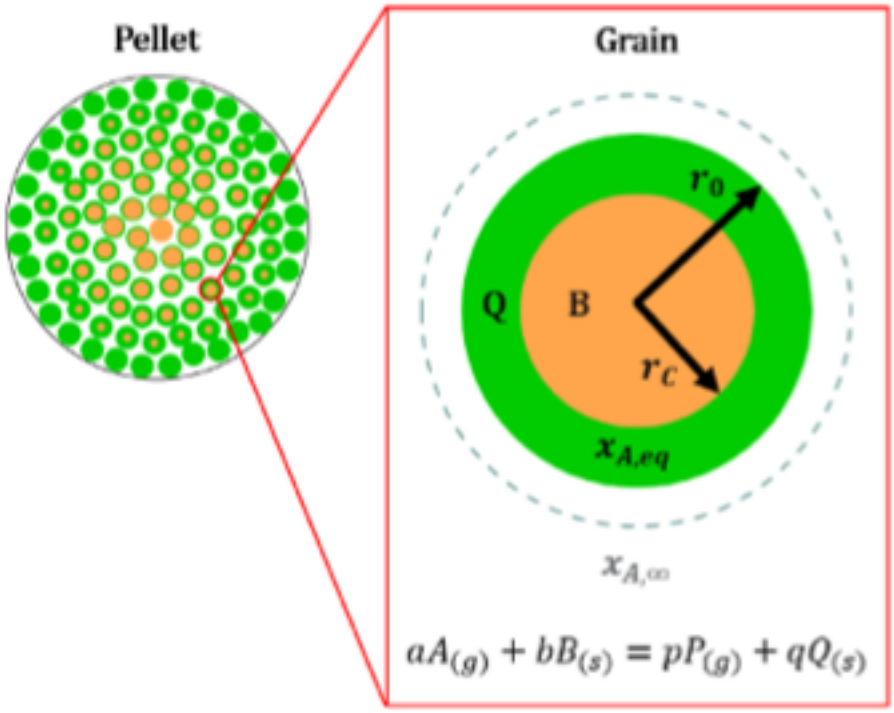

Figure 4. Grain model model applied to a generic gas-solid reaction. Here, the SCM model described previously is applied at the grain scale rather than at the pellet scale.

In the case where the reaction is isothermal and its order is one, the law of additive reaction times states that the time needed to reach a certain conversion X is given by:

$$\boldsymbol{t(X) = \tau_{chim} \cdot f(x) + \tau_{diff} \cdot g(X) + \tau_{ext} \cdot h(X)} \quad (\mathbf{eq}.21)$$

where *f, g, h* are conversion functions related to each phenomenon. Eq. 21 is exact in the case of a reaction with a reaction order of one with respect to the gas A, but Sohn (1978), and later Patisson et al. (2006), showed that it remains approximatively exact in other situations, especially if it is used in its differential form, to calculate the reaction rate by derivation. It has the great advantage to permit a direct analytical calculation of the reaction rate whereas the Grain model requires a numerical solution. We retained this approach for the SPKM.

The rate of conversion at each time is directly derived from this equation, and we can build up the conversion through numerical resolution:

$$\boldsymbol{X(t + dt) = X(t) + r_X \cdot dt} \quad (\boldsymbol{eq}.22)$$

In practice, the code solves for the mass fraction of each solid species over time with an explicit Euler scheme of order 1.

Additional carburization reactions

The presence of carbon-bearing gas (CO and CH_4) in a shaft furnace leads to the deposition of carbon on the surface of the pellets. The major contributions to this phenomenon come from the reverse Boudouard reaction and the decomposition of methane, and their kinetics both depend on the carbon activity a_c. The latter is determined by the Chipman relationship (see (H. Hamadeh, 2018)):

$$log(\mathbf{a_c}) = \frac{\mathbf{2300}}{\mathbf{T}} - \mathbf{0.92} + \left(\frac{\mathbf{3860}}{\mathbf{T}}\right)\mathbf{C} + log\left(\frac{\mathbf{C}}{\mathbf{1-C}}\right) \quad (\mathbf{eq}.23)$$

where C is the number of carbon atoms divided by the number of iron atoms.

The rate of each reaction is then given by:

$$\mathbf{r_d} = \frac{\mathbf{k_d}}{\mathbf{P_{H_2}^{0.5}}}(\mathbf{1}-\boldsymbol{\epsilon}_{\mathbf{bed}})(\mathbf{1}-\boldsymbol{\epsilon}_{\mathbf{grain}})\left(\mathbf{P_{CH_4}} - \frac{\mathbf{a_c} * \mathbf{P_{H_2}^2}}{\mathbf{K_{eq,d}}}\right) \quad (\mathbf{eq}.24)$$

$$\mathbf{r_B} = (\mathbf{k_B}\boldsymbol{P_{H_2}^{0.5}} + \boldsymbol{k'_B})\left(\mathbf{P_{CO}^2} - \frac{\mathbf{a_c} * \mathbf{P}_{\boldsymbol{CO_2}}}{\mathbf{K_{eq,B}}}\right) \quad (\mathbf{eq}.25)$$

where ϵ_{bed} and ϵ_{grain} are the porosities of the bed and the grains, respectively, the gas pressures are given in bars, and k_d, k_B, k'_B, are derived from (H. Hamadeh, 2018).

3. Results

3.1. Grain and powder bed model

It was found that the grain and bed model outlined in section 2.1 could qualitatively reproduce the overall changes in the gas composition measured by the TCD and by gas chromatography in the reduction experiments at AAU, including plateaus and slope changes of the curves caused by the stepwise reduction process from hematite through magnetite and wustite to metallic iron, in combination with chemical equilibrium limits. During some parts of the reduction experiments, the hydrogen content of the gas often became so low in the lower part of the bed that it could not reduce the wustite in this region, yielding a constant overall reaction rate.

Figure 5 present an example of the simulated (normalized) thermal conductivity of the gas leaving the bed at four different temperatures (600-900°C), showing striking resemblance with the experimental results (see Deliverable 1.1). The characteristic shape of the curves was found to change with the conditions, largely reflecting the stability of the iron oxides and equilibrium constraints, as indicated in the figure, where the "kinks" in the curves occur when the reduction of an iron oxide ends. This demonstrates nicely how the model can be used to interpret results from the bed reduction experiments and explain even detailed features of the reaction system studied.

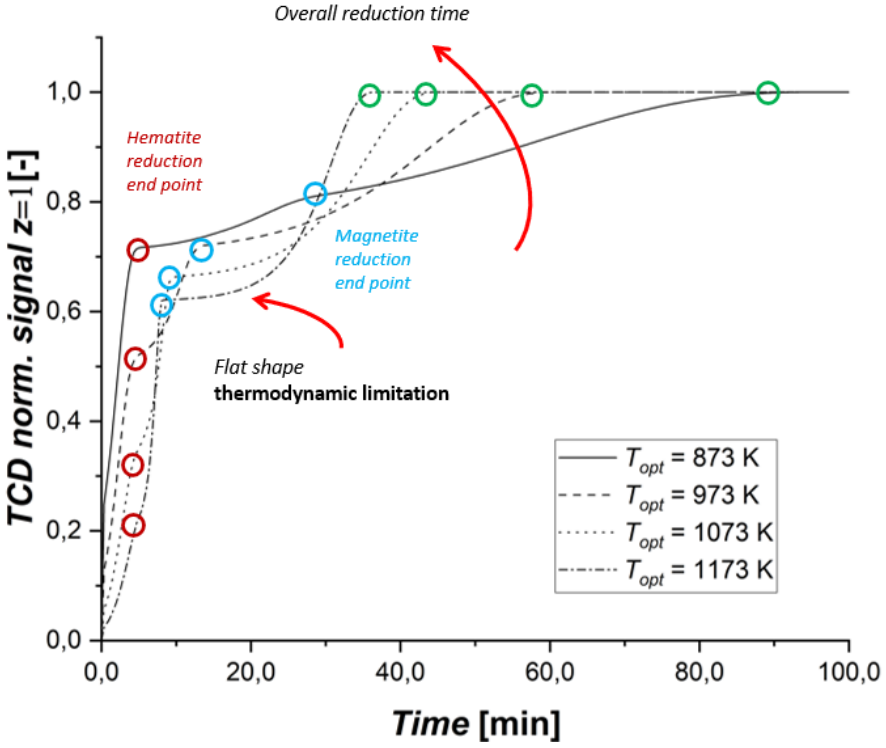

Figure 5. Simulated thermal conductivity of the gas leaving the sample bed, normalized by the conductivity of the entering gas, for four different operating temperatures.

Figure 6 presents a detailed view of the simulated conditions in a 100 mg bed during a reduction experiment at 650°C with 20% hydrogen in the feed gas, illustrating the spatial and temporal distribution of iron oxides and iron (bottom row). Hematite is seen to be reduced throughout the bed almost immediately, magnetite within 25 minutes and wustite within 65 minutes, with a step-wise response of the simulated (normalized) signal from the TCD device (top right). The figure also shows how the gas concentration profiles in the bed (top left) evolve with time.

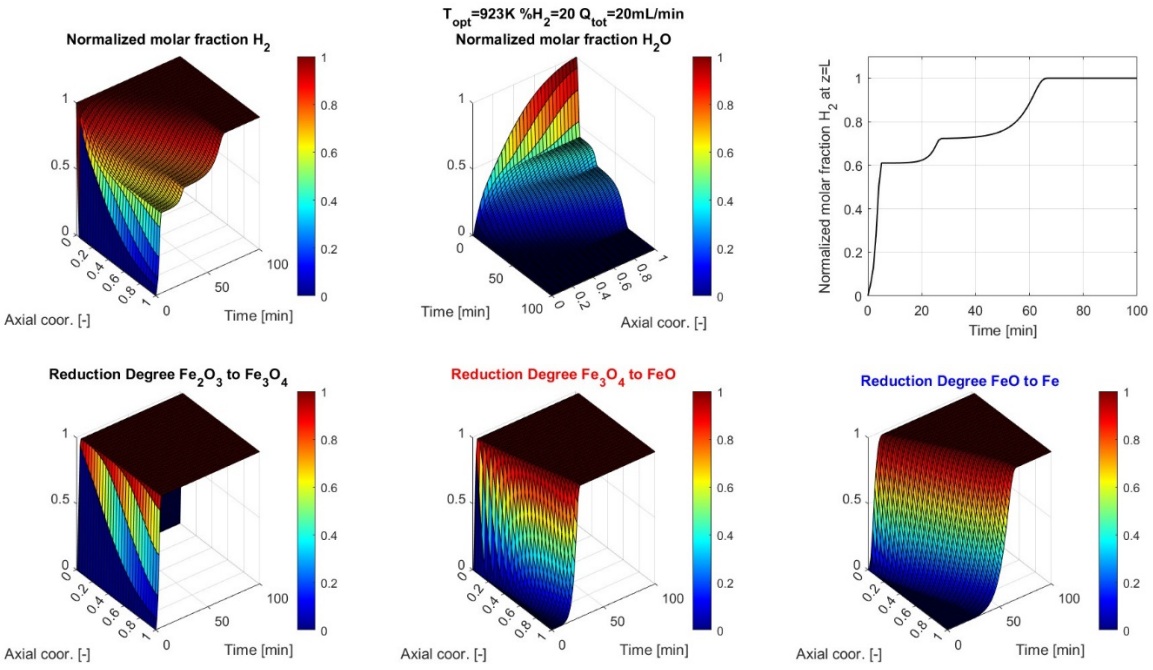

Figure 6. Spatial and temporal distribution of gas and solid components for a simulated bed reduction experiment at 650 °C with 20% of hydrogen in the feed gas.

The following paragraphs illustrate the sensitivity of the model to changes in some key parameters for a system at 600 °C with 100 mg bed to which a gas flow of 20 ml/min is fed. Unless differently reported, the feed concentration of hydrogen was 20%.

While the pre-exponential factors in the kinetic expression (eq. (5) above) for the hematite-to-magnetite and magnetite-to-wustite reactions affect the results locally and insignificantly, the factor for the wustite-to-metallic iron step considerably influences the progress of the reactions, as seen in Figure 7. Here, the factor was varied in the range $k_{3,\mathrm{ref}} = 1 \ldots 10 \cdot 10^{-5}\ \mathrm{m/s}$, which is seen to change the time to complete reduction by almost 100 minutes. This is logical since the wustite reduction reaction is known to be the rate-limiting step, but it is interesting to see how the appearance of the thermal conductivity curve changes. For the lowest $k_{3,\mathrm{ref}}$ value studied, there is no plateau in the curve which instead rises almost linearly during the last reduction step. The reaction is here so slow that the gas composition never reaches the equilibrium limit.

The feed concentration of hydrogen obviously plays an important role for the reduction rates. Figure 8 shows the results when the feed concentration is increased from 10% to 30% in steps of 5% points. This shortens the time to reach total reduction from 160 min to about 50 min.

As a final illustration example, the impact of the total gas flow rate is studied, varying it from 10 ml/min to 30 ml/min. Since the hydrogen content of the feed gas is constant (20%), a higher total flowrate brings more hydrogen to the bed making it react more readily. By contrast, a low total flow rate leads to hydrogen starvation in the lower parts of the bed, which prolongs the “plateaus” and the time to full reduction of the bed.

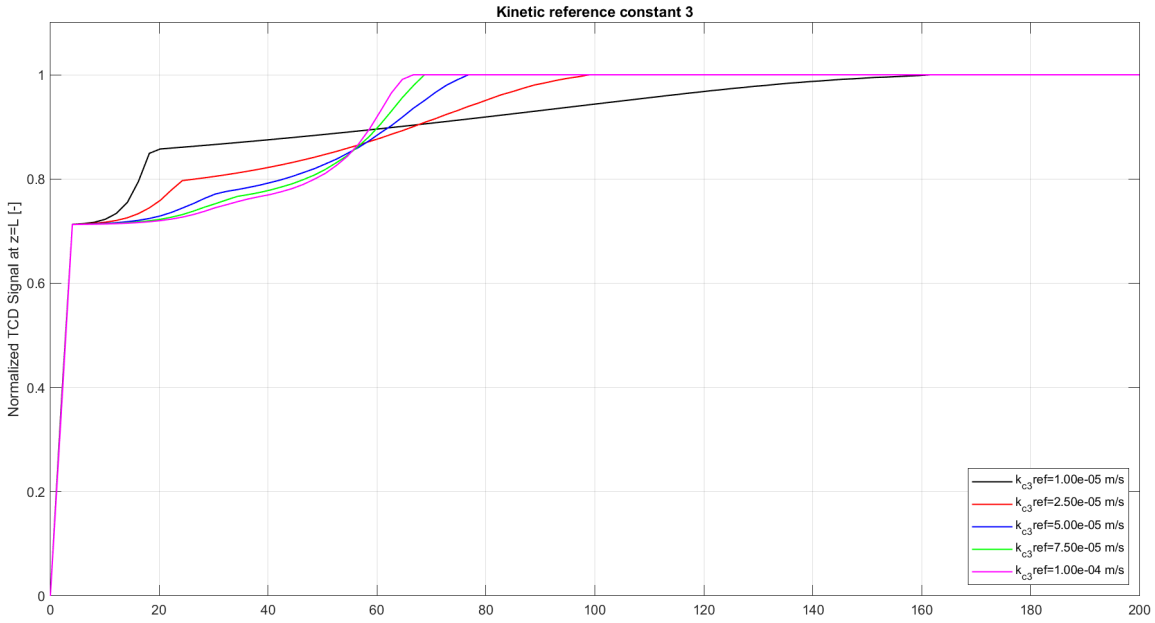

Figure 7. Simulated (normalized) thermal conductivity of the gas leaving the sample bed for different values of the pre-exponential factor (cf. eq. (5) above) of the wustite reduction reaction.

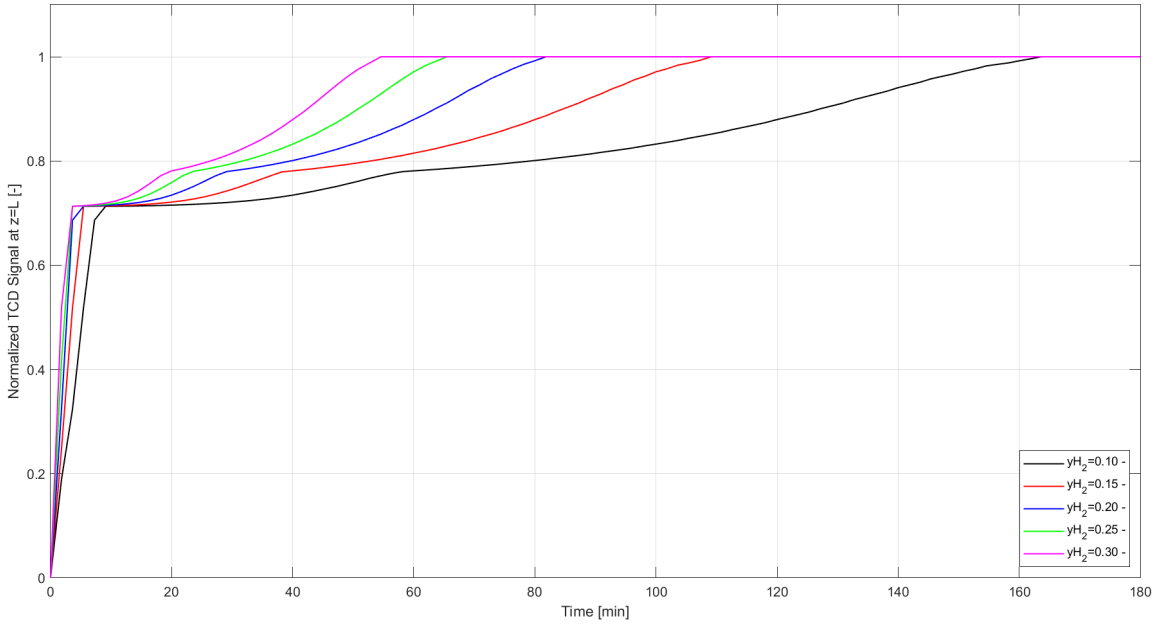

Figure 8. Simulated (normalized) thermal conductivity of the gas leaving the sample bed for different values of the hydrogen concentration of the feed gas.

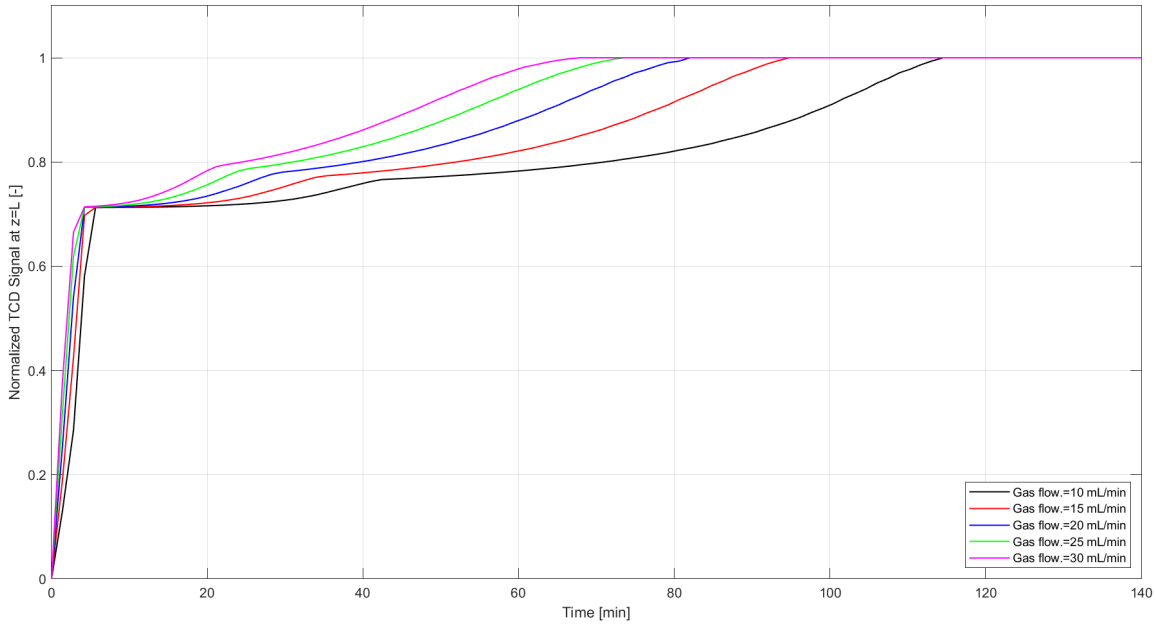

Figure 9. Simulated (normalized) thermal conductivity of the gas leaving the sample bed for different values of the feed gas flow rate.

The overall trends predicted by the grain and powder bed model have been found to coincide quite well with the findings from the chemisorption reduction experiments. A sensitivity analysis of the model has revealed important parameters for the predicted reduction behaviour. Still, the model parameters have thus far been given quite arbitrary values and should in forthcoming work be tuned. This will be done in a parameter estimation phase where the model is applied iteratively in a search for an optimal set of parameter values for which the differences between the observed and simulated outlet gas compositions are minimized.

In a preliminary attempt to explore the feasibility of this approach, a limited set of model parameters were manually tuned to make the predicted thermal conductivity of the outgoing gas follow the measured counterpart. Figure 10 shows the results of a reduction test (circles) and the fit provided by the model (solid line) after adjusting the pre-exponential constants $k_{j,\mathrm{ref}}$ and the axial dispersion coefficient D_z. The model shows nice flexibility, which holds promise for a successful forthcoming parameter estimation phase in the project.

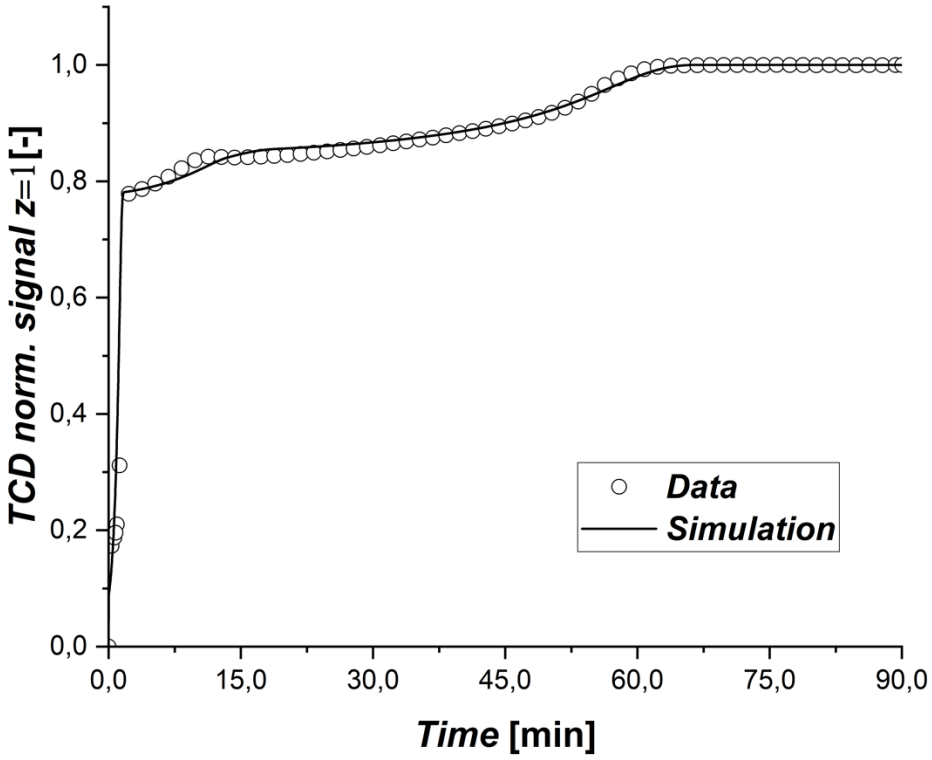

Figure 10. Measured (normalized) thermal conductivity of the gas leaving the sample bed (o) and the prediction by the model (—) after tuning a limited set of parameters.

3.2. Kinetic model of a single pellet

Note: The code of SPKM has been made available in the MaxH2DR share point for all members of the project (here).

3.2.1. Numerical implementation

UL previously developed a subroutine built upon the Grain model in the CFD code Reductor, a shaft furnace simulator. In MaxH2DR, a new, open version of this kinetic model of a single pellet is being developed, designed to be shared with the partners. It is written in Python.

This new stand-alone model can be used with different targets:

- simulate the behaviour of one pellet under constant external conditions (like a pellet undergoing a reduction experiment in a thermobalance) or variable external conditions (like a pellet descending in a DR shaft furnace),
- determine kinetic constants from curve fitting between calculated and measured data,
- be integrated in a multiparticle reactor model.

These three capacities will be used in MaxH2DR.

In the case of the reduction of iron oxides, we can calculate the reaction rate of each sub-reaction (all listed below) and the corresponding reaction extents through the methodology explained above. This must be done carefully, since H_2 and CO are competitors in the reduction of oxides. Thus, we continuously calculate each τ_i, t_i, r_i and X_i as they directly determine the overall reduction reaction extent through:

$$\boldsymbol{X = \frac{1}{9}X_1 + \frac{32}{171}X_2 + \frac{40}{57}X_3} \quad (\boldsymbol{eq}.26)$$

This is particularly interesting for comparison with reduction experiments, since thermobalances allow only for the measurement of the global reaction extent, and not the extent of each sub-reaction.

In the current version of the code, the following assumptions are made:

- Gas properties such as molar fractions of species, pressure and gas flow do not change during the reduction. The overall temperature is kept constant since the reduction is assumed to be isothermal at the pellet scale.
- The thermodynamic data are taken from the database COACH, which comes from the software Gemini (Thermodata Europe). Kinetic parameters have been determined in previous works from (Costa, La réduction du minerai de fer par l'hydrogène : étude cinétique, phénomène de collage et modélisation, 2011). Gas viscosity is taken from literature, and gas binary diffusion coefficients are calculated according to the Chapman-Enskog theory.
- On the solid sample side, the most influent solid sample characteristics (grain and pores diameter, initial composition, specific surface area, pellet apparent density) can be directly measured through experiments (SEM, BET, pycnometry, for instance). Porosity is considered both between the grains (ε_{inter}) and inside those grains (ε_{intra}) – the variation of porosity is calculated based on the difference of molar volumes between the different iron oxides.

The code also includes two carbon deposition reactions (listed below) – the methane decomposition reaction and the reverse Boudouard reaction. Their respective kinetic constants are taken from a previous work (H. Hamadeh, 2018). As the decomposition of methane is catalysed both by temperature and iron content, we set a minimum value for each of these parameters to allow the reaction to take place (the temperature must be above 773 K and the mass fraction of iron above 0.4)

Below are listed the reactions considered in the code (the first 6 reactions are related to the reduction of oxides with H_2 and CO, while the 2 last ones describe the carbon deposition):

$$\mathrm{i} = 1: \quad 3\mathrm{Fe_2O_3} + \mathrm{H_2} \rightarrow 2\mathrm{Fe_3O_4} + \mathrm{H_2O} \quad (\mathrm{eq}.27)$$

$$\mathrm{i} = 2: \quad \mathrm{Fe_3O_4} + \frac{16}{19}\mathrm{H_2} \rightarrow \frac{60}{19}\mathrm{Fe_{0.95}O} + \frac{16}{19}\mathrm{H_2O} \quad (eq.28)$$

$$\mathrm{i} = 3: \quad Fe_{0.95}O + H_2 \rightarrow 0.95Fe + H_2O \quad (\mathrm{eq}.29)$$

$$\mathrm{i} = 4: \quad 3Fe_2O_3 + CO \rightarrow 2Fe_3O_4 + CO_2 \quad (\mathrm{eq}.30)$$

$$\mathrm{i} = 5: \quad Fe_3O_4 + \frac{16}{19}CO \rightarrow \frac{60}{19}Fe_{0.95}O + \frac{16}{19}CO_2 \quad (\mathrm{eq}.31)$$

$$\mathrm{i} = 6: \quad Fe_{0.95}O + CO \rightarrow 0.95Fe + CO_2 \quad (\mathrm{eq}.32)$$

$$\mathrm{CH_4} \rightarrow \mathrm{C} + 2\mathrm{H_2} \quad (\mathrm{eq}.33)$$

$$2CO \rightarrow C + CO_2 \quad (\mathrm{eq}.34)$$

Among the many challenges to implement the model, one detail is worth mentioning – the availability of solid reactant for each reaction. Since the product of the first and second reactions of reduction are also reactants for the second and third ones, the latter should not be allowed to consume more reactant that is already available. That is why maximum reaction extents for the second and third stages of iron oxide reduction (that is, the reduction of magnetite and wustite) are defined. We give an example below :

*

Let us consider the second reaction of reduction $(Fe_3O_4 \rightarrow Fe_{0.95}O)$ *.* r_2 *and* r_5 *are calculated with the characteristic times defined above, and the value of* X_2 $(= X_5)$ *from the previous iteration. We should be able to write :*

$$X_2(t + dt) = X_2(t) + dt * (r_2 + r_5)$$

But at time $t + dt$*, one can not consume more magnetite than what is available at time t and what is currently created through the first reduction reaction. That is, we must always ensure that*

$$X_2 <= X_1$$

*

Examples of output graphs obtained with the code are given below. A desired use of the code can be e.g. the comparison of the reduction kinetics of one pellet at different temperatures, keeping all other parameters constant (see). Another one can be, for a specific experiment, to thoroughly explore, and draw the evolution of phases, reaction rates, limiting rate processes, etc. Figure 44 shows the results for phase evolution.

3.2.2. First results

The first thing to notice is that our model does not currently take into account the differences in pellet material, except through the initial chemical composition. It has been built with data coming from measurements on the CVRD (D) pellets, and this is why the majority of the simulations that follow only concern this type of pellets.

Typical results for the reduction of CVRD (D) pellets are given in Figure 11 and

Figure 12, for an industrial gas mix. We already see a close resemblance between these simulated results and the experimental results available in Deliverable 1.1.

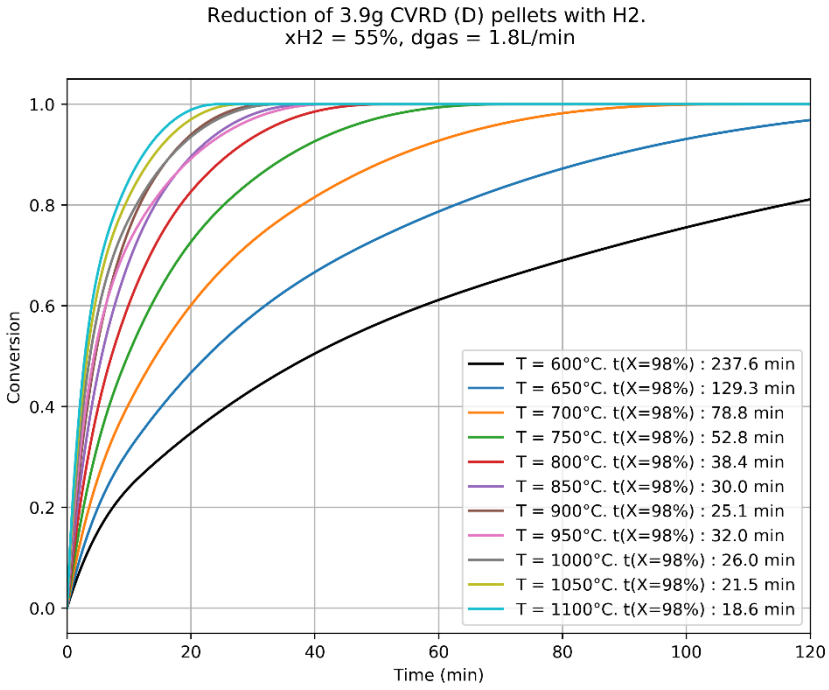

Figure 11 : Simulated reduction of CVRD (D) pellets in the (600-1100)°C temperature range. The global T dependency and the kinetic slowdown at 950°C can already be distinguished here.

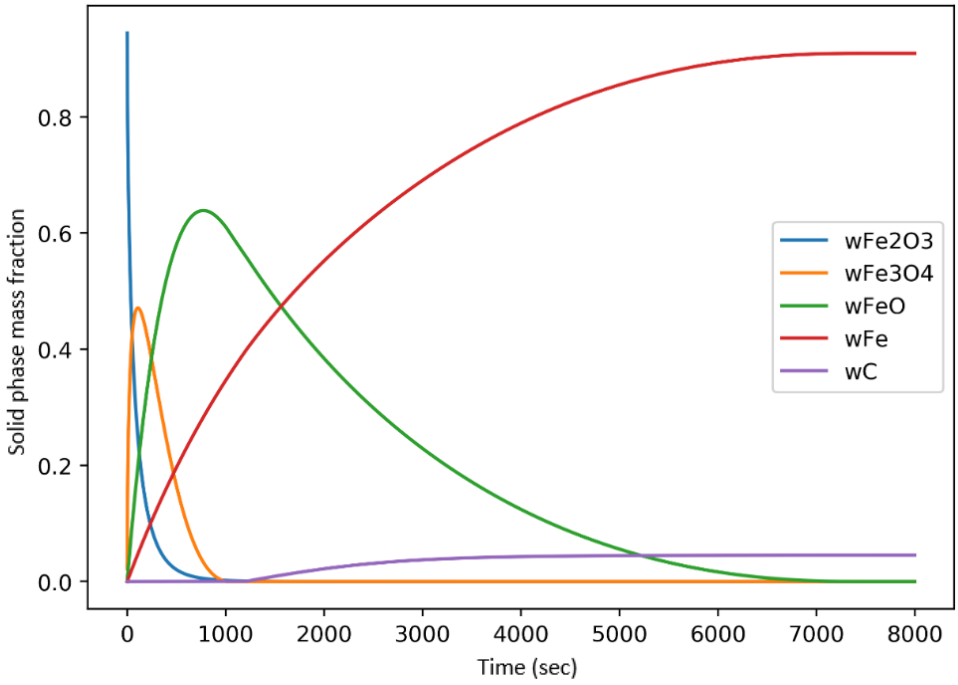

Figure 12 : Simulated phase evolution during the reduction of a CVRD (D) pellet with an industrial gas mix. The deposition of carbon is activated by the presence of pure reduced iron in the pellet.

Simulation vs experiments : the case of Temperature

The best agreement between model and experiments was obtained in the 750-900 °C temperature range, which is the nominal range of temperature encountered in DR shaft furnaces. There, we observe a nice agreement on the shape of the reduction curves as well as on the characteristic time of reduction $t_{98} = t(X = 98\%)$, as can be seen on Figure 13 and Figure 14. But even though our model takes into account the kinetic slowdown observed at 950 °C (through solid diffusion of oxygen atoms through the dense iron layer), the resulting simulation does not agree well with the experimental curve, so that it underestimates the time it takes for an 98% reduction (34 min for the simulation , 44 min for the experiment). The simulated kinetic slowdown is too marked at the beginning and not enough at the end. This should still be improved, further experiments and subsequent modelling are planned in this respect.

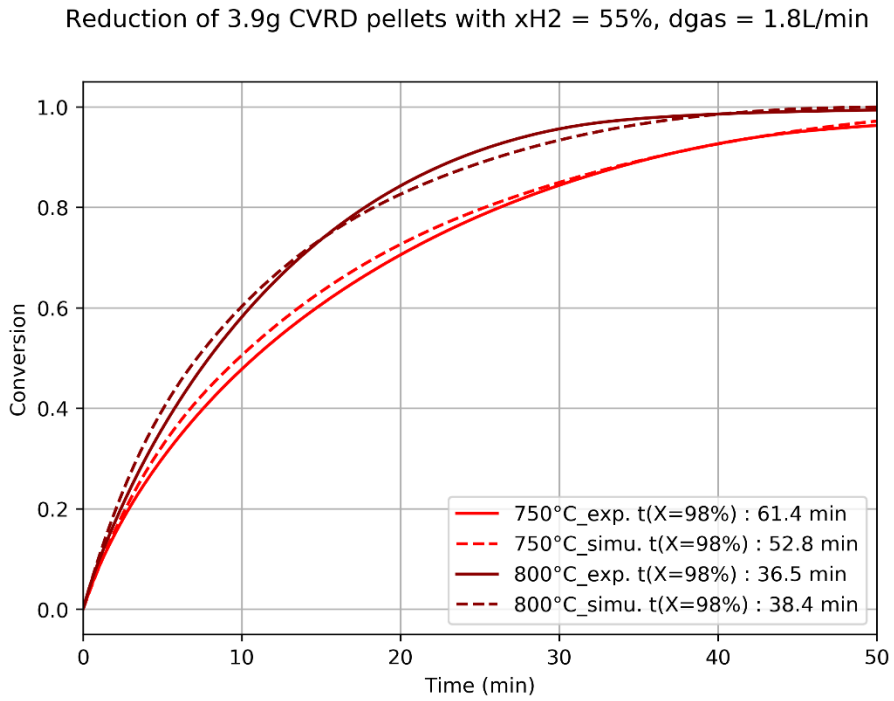

Figure 13 : Comparison of simulated and experimental results for the reduction of CVRD (D) pellets at 750 and 800°C.

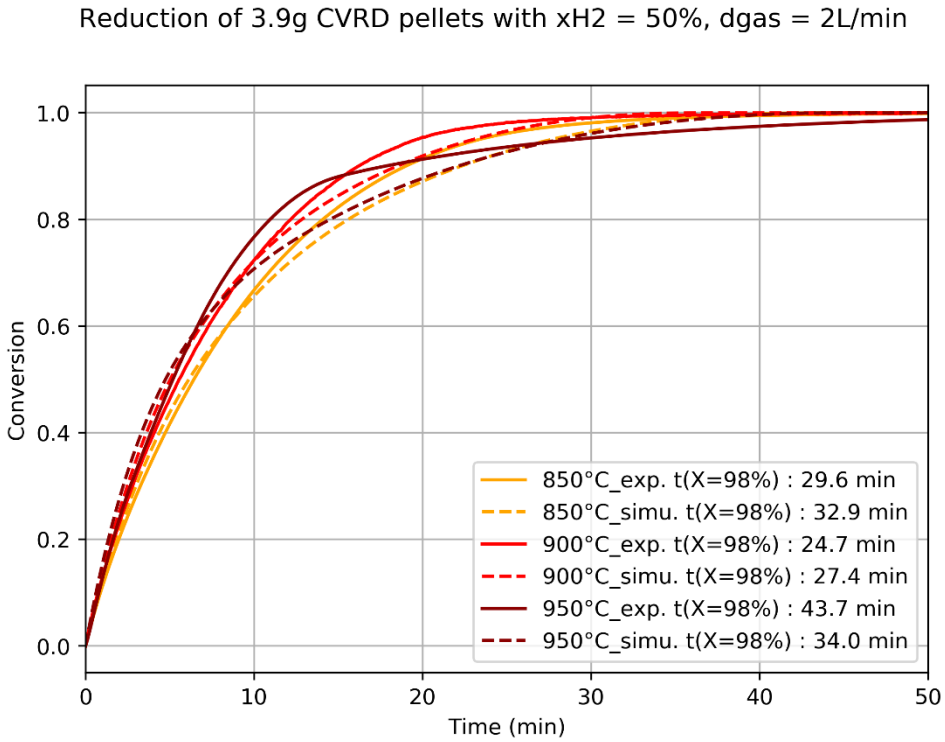

Figure 14 : Comparison of simulated and experimental results for the reduction of CVRD (D) pellets at 850, 900 and 950°C.

At higher temperatures, above 1000 °C, the model overestimates t_{98}. This is because the reduction mechanisms are not quite the same. Wide-open cracks have been observed above 1000 °C – if these appear during reduction, they could lead to faster reduction at higher conversions (for the second and third reduction reactions), which could explain the higher speed of reduction in experiment than in simulations (see Figure 15).

Finally, at lower temperatures ($T < 700°C$), it seems that r_2 and r_3 are underestimated since the simulated reaction curves deviate from the experimental ones at the intermediate and final stages of reduction (see Figure 16). This range of temperature was not considered in former studies and further interpretation of the results is necessary.

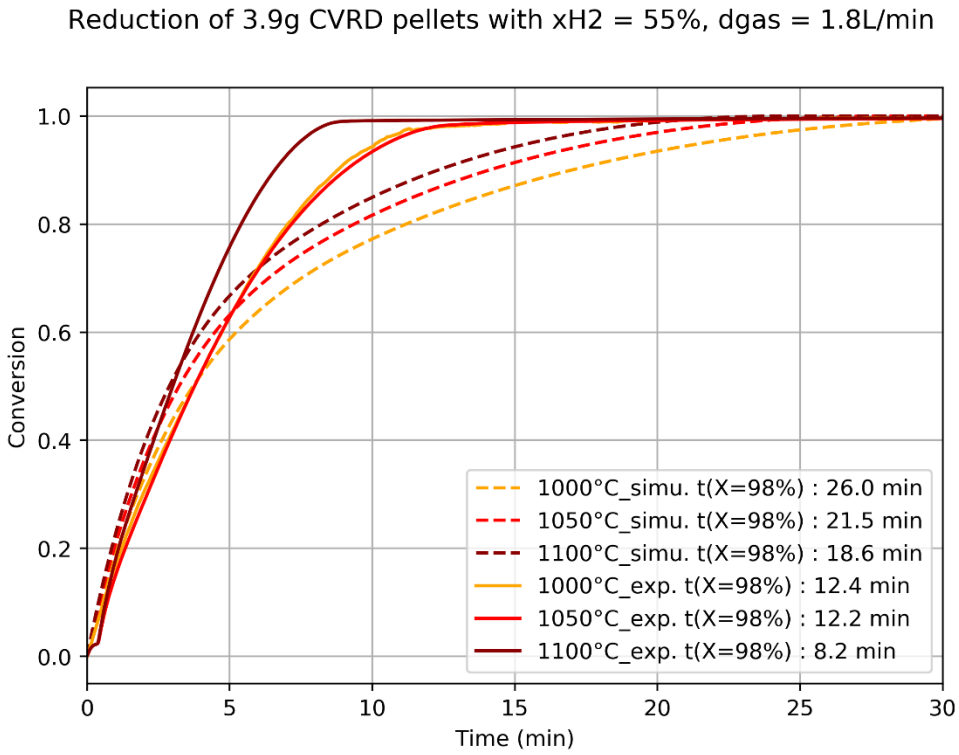

Figure 15. Comparison of simulated and experimental results for the reduction of CVRD (D) pellets at 1000, 1050 and 1100 °C.

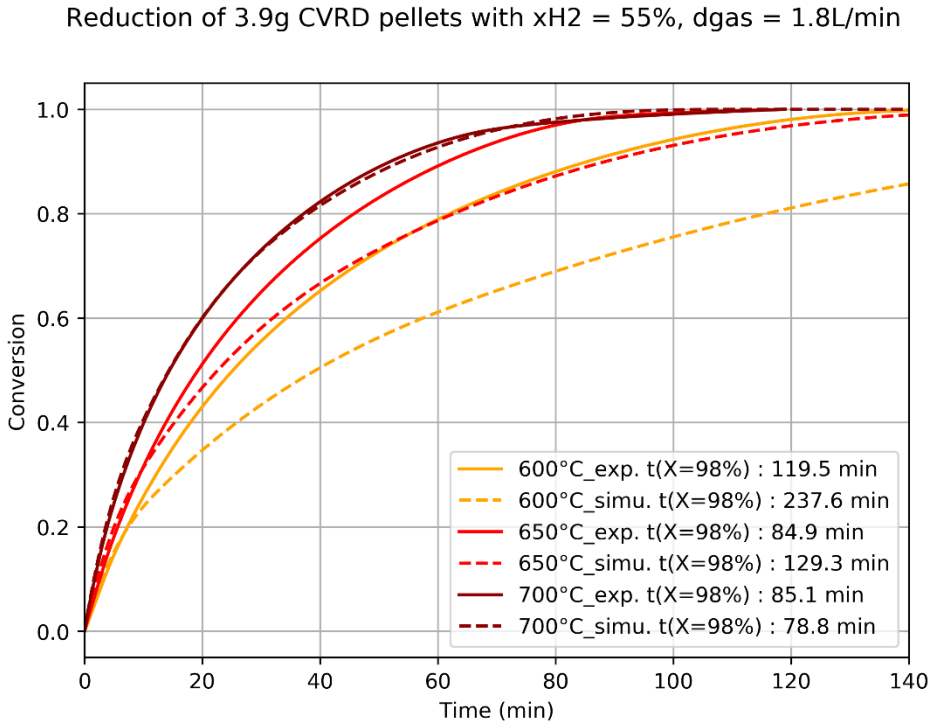

Figure 16. Comparison of simulated and experimental results for the reduction of CVRD (D) pellets at 600, 650 and 700°C.

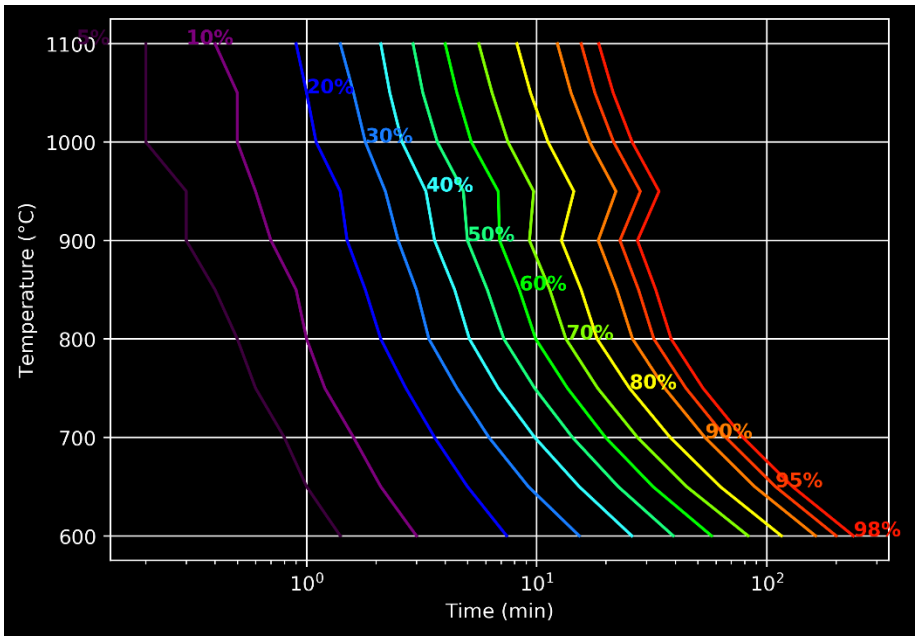

Figure 17 : TTT diagram drawn from the simulation of the reduction of CVRD (D) pellets, in the (600-1100) temperature range. xH2 = 50% and dgas = 2L/min for $\mathbf{850°C} \leq T \leq \mathbf{950°C}$; xH2 = 50% and dgas = 2L/min otherwise.

Simulation vs experiments : the case of Dilution

The effect of dilution is quite similar between the simulated and experimental results, i.e. it slows down the reduction without changing the apparent behaviour (and thus mechanisms) of the reduction. This is visible on Figure 18 and especially on Figure 19.

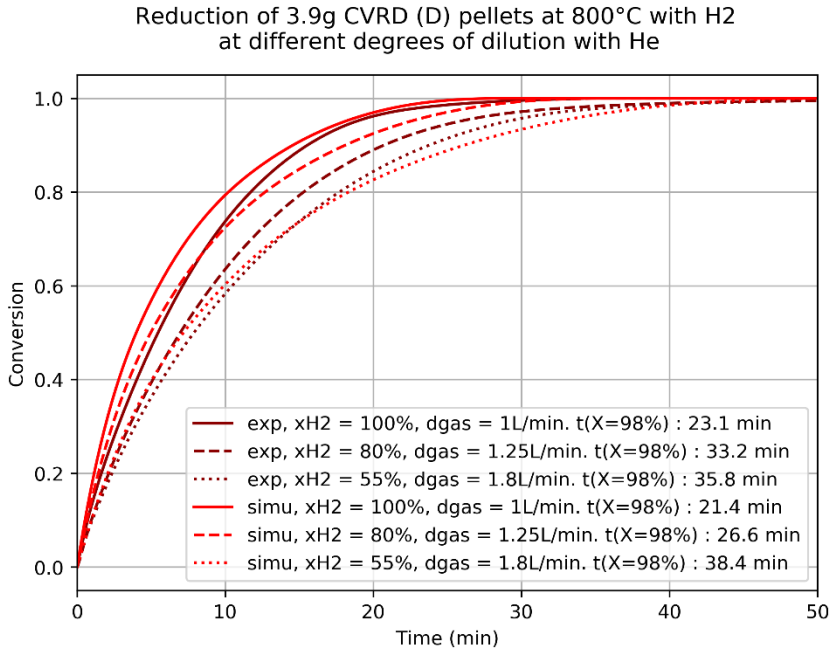

Figure 18 : Comparison of simulated and experimental results regarding the effects of hydrogen dilution in helium on the conversion. Simulations are drawn in red and experiments in dark red.

All in all, the model gives quite satisfactory results, especially in the medium temperature range (750-900°C). It has been incorporated in the REDUCTOR code to simulate existing shaft furnaces with great success.

We should now turn ourselves towards experiments with CO and CH4 to see if the model properly describe the carbon reduction and the carbon deposition reactions. The code could also be further developed by introducing variable external conditions (gas temperature and composition) in order to be able to simulate the first moments of a TG experiment, as well as the evolution along a DR furnace.

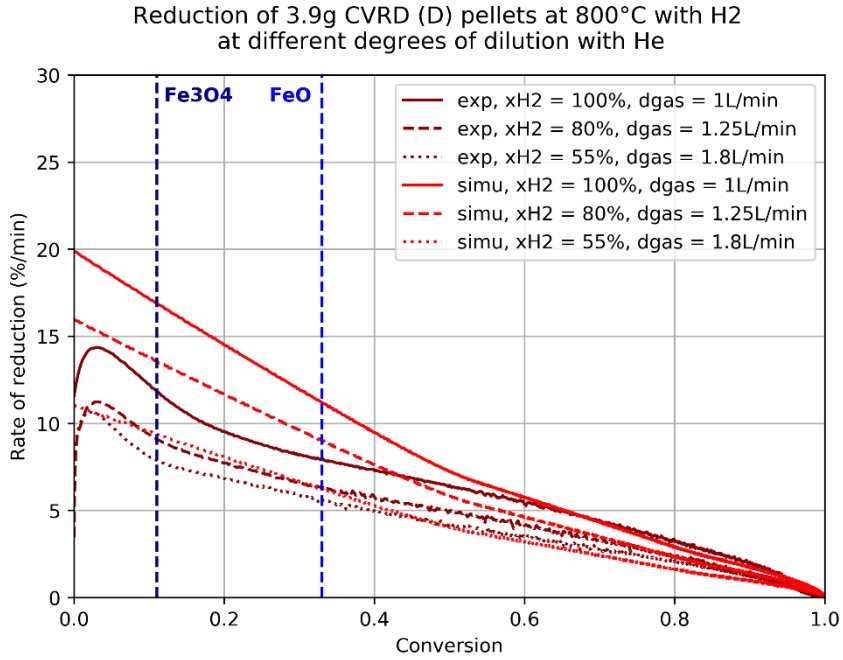

Figure 19 : Comparison of simulated and experimental results regarding the effects of hydrogen dilution in helium on the rate of reduction. Simulations are drawn in red and experiments in dark red.

4. Conclusion

Two models have been developed to describe the reduction of iron oxides with a reactant gas. Both were necessary since they model different situations: the case of a bed of fine grains and that of a single pellet. Indeed, the fronts between the intermediate oxides behave differently in a grain, a grain bed and a pellet.

The dynamic bed model proposed by AAU, based on the SCM and 1D transient mass balances on the scale of the bed gives quite satisfactory results to explain and predict the behaviour of oxide or ore grains in chemisorption experiments. A sensitivity analysis of the model has revealed the key parameters by which the model can be tuned to the experimental observations. A challenge will be how to limit the number of parameters to be estimated to obtain unique results and how to adapt to changes in the material structure that the SCM may have limited ability to capture using the present model formulation. Another challenge is how accurately the grain-size distribution of the powder can be described in the model.

The single pellet kinetic model built by UL, based on the law of additive reaction times, gives quite satisfactory results for the simulation of a pellet reduced in a thermobalance between 750 and 950°C, which is the usual range of temperature encountered in DR shaft furnaces. The lower agreement at higher and lower temperatures will be improved by modifying some features, like the description of the kinetic slowdowns. The SPKM has been made available to the other partners of MaxH2DR. It is already tested by BFI for instance.

Both teams are now going to refine the kinetic parameters through mathematical optimization (curve fitting between calculated and measured data). The models will then be implemented in the DR shaft models of MaxH2DR consortium (in fact they already started to be).

5. References

(in order of appearance in the text)

E. Salucci, A. D'Angelo, V. Russo, H. Grénman, H. Saxén, Modelling of iron oxide reduction with hydrogen in a small fixed bed, Chemical Engineering Science (2024), doi: https://doi.org/10.1016/ j.ces.2024.119934

J. Szekely, J.W. Evans, H.Y. Sohn, Gas-solid reactions, Academic Press, New York, 1976.

D.R. Parisi, M.A. Laborde “Modeling of counter current moving bed gas-solid reactor used in direct reduction of iron ore”, Chemical Engineering Journal, (2004), 104, 35–43.

Q.T. Tsay, W. H. Ray, J. Szekely “The modeling of hematite reduction with hydrogen plus carbon monoxide mixtures”, AIChE Journal, (1976), 22, 6, 1064–1072.

A. Ranzani da Costa, D. Wagner, F. Patisson, “Modelling a new, low CO2 emissions, hydrogen steelmaking process”, J. Cleaner Production, (2013), 46, 27–35.

H.Y. Sohn, “The law of additive reaction times in fluid-solid reactions”, Metallurgical Transactions B, (1978), 9B, 1, 89–96.

F. Patisson, B. Dussoubs, D. Ablitzer, “Using Sohn’s law of additive reaction times for modeling a multiparticle reactor. The case of the moving bed furnace converting uranium trioxide into tetrafluoride”, Sohn International Symposium “Advanced processing of metals and

materials", 27-31 Aug. 2006, San Diego. Proceedings edited by F. Kongoli and R.G. Reddy, TMS, vol. 1 "Thermo and physicochemical principles: non-ferrous high-temperature processing", 141-153.

H. Hamadeh, O. Mirgaux, F. Patisson, "Detailed modeling of the direct reduction of iron ore in a shaft furnace", Materials, (2018), 11, 1865, 1-16.